CHEMISTRY
A EUROPEAN JOURNAL

ChemPubSoc Europe

DOI: 10.1002/chem.201203176

Understanding the Effect Models of Ionic Liquids in the Synthesis of NH_4-Dw and γ-AlOOH Nanostructures and Their Conversion into Porous γ-Al_2O_3

Xiaochuan Duan, Tongil Kim, Di Li, Jianmin Ma, and Wenjun Zheng*[a]

Abstract: Well-dispersed ammonium aluminum carbonate hydroxide (NH_4-Dw) and γ-AlOOH nanostructures with controlled morphologies have been synthesized by employing an ionic-liquid-assisted hydrothermal process. The basic strategies that were used in this work were: 1) A controllable phase transition from NH_4-Dw to γ-AlOOH could be realized by increasing the reaction temperature and 2) the morphological evolution of NH_4-Dw and γ-AlOOH nanostructures could be influenced by the concentration of the ionic liquid. Based on these experimental results, the main objective of this work was to clarify the effect models of the ionic liquids on the synthesis of NH_4-Dw and γ-AlOOH nanostructures, which could be divided into cationic- or anionic-dominant effect models, as determined by the different surface structures of the targets. Specifically, under the cationic-dominant regime, the ionic liquids mainly showed dispersion effects for the NH_4-Dw nanostructures, whereas the anionic-dominant model could induce the self-assembly of the γ-AlOOH particles to form hierarchical structures. Under the guidance of the proposed models, the effect of the ionic liquids would be optimized by an appropriate choice of cations or anions, as well as by considering the different effect models with the substrate surface. We expect that such effect models between ionic liquids and the target products will be helpful for understanding and designing rational ionic liquids that contain specific functional groups, thus open up new opportunities for the synthesis of inorganic nanomaterials with new morphologies and improved properties. In addition, these as-prepared NH_4-Dw and γ-AlOOH nanostructures were converted into porous γ-Al_2O_3 nanostructures by thermal decomposition, whilst preserving the same morphology. By using HRTEM and nitrogen-adsorption analysis, the obtained γ-Al_2O_3 samples were found to have excellent porous properties and, hence, may have applications in catalysis and adsorption.

Keywords: alumina · crystal growth · ionic liquids · nanostructures · phase transitions

Introduction

Over the past two decades, since the discovery of water-stable ionic liquids by Wilkes and Zaworotko in 1992, ionic liquids (ILs) have found widespread application in organic chemistry and organometallic catalysis, whilst their use in inorganic synthesis is quite new.[1–10] The use ionic liquids instead of water as the solvent for the synthesis of inorganic materials was pioneered by Dai et al. in 2000.[11] They introduced ILs for the synthesis of porous silica gels, termed "ionogels", which are now being extensively investigated. Subsequently, the use of ionic liquids has been actively attempted for the preparation of a broad range of inorganic materials and many interesting inorganic structures with various properties have been fabricated. Notably, Dupont et al. prepared uniform Ir nanoparticles in ionic-liquid media.[12] Nakashima and Kimizuka reported the synthesis of hollow titania microspheres in a toluene/ionic-liquid medium.[13] Zhou and Antonietti obtained spherical TiO_2 aggregates that were composed of nanoparticles by using an ionic liquid.[14] Correspondingly, the "ionothermal" and "all-in-one" concepts for the synthesis of materials by using ionic liquids as the solvent were proposed by Morris and co-workers and Taubert in 2004, respectively.[15,16] Notably, ionothermal synthesis is quite different from hydro- or solvothermal conditions and it may lead to new materials with interesting morphologies that are not accessible by using conventional organic solvents or water, owing to the unique physicochemical properties of ionic liquids.[17–19] Despite the great efforts that have been made in controlling the crystal phase and morphology of inorganic materials by using an ionic liquid, a consensus on the type of effect between the ionic liquid and the substrate has still not been reached. As a consequence, most of the syntheses cannot be predicted and simply use an IL or a mixture of an IL with a conventional solvent, just like a common surfactant, which does not sufficiently exploit the main advantages of ILs. There are two main reasons that have led to this situation: 1) A molecular-

[a] Dr. X. Duan, Dr. T. Kim, Dr. D. Li, Dr. J. Ma, Prof. Dr. W. Zheng
Department of Materials Chemistry
Key Laboratory of Advanced Energy Materials Chemistry and
TKL of Metal and Molecule-Based Material Chemistry
College of Chemistry, Nankai University
94 Weijin Road, Tianjin, 300071 (P.R. China)
Fax: (+86) 022-23502458
E-mail: zhwj@nankai.edu.cn

Supporting information for this article is available on the WWW under http://dx.doi.org/10.1002/chem.201203176.

based understanding of the physicochemical properties of ILs is a great challenge because different ionic liquids have different physicochemical properties and reliable parameters are sometimes not available; as such, the construction of a systematic database of the physicochemical properties of ILs is an urgent requirement; 2) the research on well-established rules and correlations between the molecular structures of the adopted ionic liquids and the morphologies of the resulting inorganic materials is limited. We believe that the determination of general trends may be utilized in the rational design of desired inorganic materials with the desired polymorph and desired morphology by using ILs.

ILs cannot be regarded as merely "green" alternatives to conventional organic solvents. Rather, the most important advantage of using ILs for the preparation of inorganic materials is that ILs form extended hydrogen-bond systems in the liquid state and, therefore, are highly structured, which can be a definition of supramolecular fluids.[2] This structural organization means that ILs can be used as entropic drivers for the generation of well-defined nanostructures with extended order. Considering that ILs contain both cations and anions, to obtain a molecular-level perspective of this structural organization, an answer to the simple question which ions (cations or anions) are closest to the liquid/solid interface between ILs and resulting materials must first be obtained.[5] However, this question is not easy to answer, although great efforts have been made through related experiments or computer simulations. Several studies have suggested that the cationic species of ILs can interact with nanoparticles and stabilize them. Finke and co-workers reported that imidazolium-based ILs can react with Ir nanoparticles to form surface-attached N-heterocyclic carbenes that contribute to the stabilization of Ir nanoparticles.[20] Similarly, Bockstaller and co-workers prepared Au nanorods in 1-ethyl-3-methylimidazolium ethylsulfate ([Emim][ES]) without the need for additional stabilizing agents. They proposed that the imidazolium cations had different binding affinities to different crystal facets of the Au nanoparticles, thereby resulting in the formation of Au nanorods.[21] Furthermore, Bouvy et al. systematically investigated the effect of the cation in pyrrolidinium-based ILs on the resulting morphologies of the Au nanostructures.[22] Previously, we have demonstrated that the interactions between imidazolium cations and TiO_6 octahedra could be a decisive factor in the formation of the rutile phase.[23] On the other hand, anionic species of ILs can also interact with nanoparticles and play an important role in the growth stage. Zhou et al. successfully synthesized mesoporous SiO_2 by using 1-butyl-3-methyl-imidazolium tetrafluoroborate ([Bmim][BF_4]) as the template and they proposed that hydrogen bonds that were formed between the $[BF_4]^-$ ions and the SiO_2 surface, together with π–π stacking interactions of the neighboring imidazolium rings, led to the mutual packing and formation of mesoporous SiO_2.[24] Taubert and co-workers also observed a strong effect of the anion in imidazolium-based ILs on the formation of Au nanoparticles, including their shape and size.[25] Hong and co-workers indicated that hydrogen bonding could occur at the interface between the anions of [C_{16}mim]Cl and building blocks of aluminum hydroxides in the synthesis of large-mesoporous γ-Al_2O_3.[26] In addition, Dupont proposed a coordination model that was composed of semi-organized $[(DAI)_m(X)_{m-n}]^{n+}[(DAI)_m(X)_{m-n}]^{n-}$ supramolecular aggregates on the formation of nanoparticles.[10] Similar conclusions were drawn by Sieffert and Wipff, based on molecular dynamics (MD) simulations of 1-butyl-3-methylimidazolium octylsulfate ([Bmim][$OcSO_4$]) near a quartz surface.[27] They concluded that the imidazolium ring and the octyl chain of the anion preferred to align near and parallel to the surface. These findings are very useful in understanding the type of effect of ILs on the formation of nanostructures with different morphologies, despite the fact that the synthetic mechanisms in the different cases are not fully clear.[28–39] We expect that this understanding will improve with the accumulation of knowledge and systematic experimentation.

Of the various non-noble metals or transition-metal oxides that have been studied, alumina, with its diverse range of crystal structures, enjoy pride of place because its physical and chemical properties and its wide applications in catalysis, ion exchange, adsorbents, and ceramics.[40–43] As the low-temperature metastable polymorph of alumina, γ-Al_2O_3, which contains a wide range of surface hydroxy groups, is one of the most important oxides and also the most common form of activated alumina for adsorptive and catalytic applications. Considering that adsorptive and catalytic processes take place on the surface, the textural properties of γ-Al_2O_3 play a critical role in determining its function. Although amorphous aluminas can exhibit surface areas of up to 800 m^2g^{-1}, their application in catalytic processes that require high-temperature environments has been hindered by their poor thermal stability. Improving the crystallinity is considered to be an effective way to enhance the thermal stability; however, crystalline γ-Al_2O_3 usually has low surface areas and poor pore properties.[40] Therefore, the synthesis of γ-Al_2O_3 with precise control over its surface area, pore properties, and thermal stability is still a great challenge. Typically, γ-Al_2O_3 nanostructures are synthesized through chemical/thermal conversion by employing aluminum carbonates, hydroxides, hydroxyoxides, and so forth as solid precursors. Well-defined nanostructures of alumina with different dimensionalities, such as nanorods, nanowires, nanotubes, and hollow and porous nanostructures, have been successfully obtained by using a series of solution-based routes and vapor-phase processes.[44–53] However, such methods require that either the template/surfactant/substrate be thoroughly removed to purify the product or that the reaction be conducted at elevated temperatures. Most importantly, γ-Al_2O_3 nanostructures may then lose many of their active sites, as a result of surface reconstruction. Thus, there remains much interest in exploring simpler and more-versatile synthetic routes that allow better control of the morphologies and structures of the nanomaterials. In this regard, ionothermal synthesis, or ionic-liquid-assisted synthesis, is widely considered to be a "green" synthetic route

because the ionic liquids can be easily removed after washing with distilled water or anhydrous alcohol without requiring complex treatments.

Considering that the morphologies of the final products are normally similar to those of the precursors, it is necessary to study the controllable synthesis of precursors with the desired morphologies. However, until now, the synthesis of uniform crystalline particles of compound intermediates remains a challenging—but less-studied—area in nanomaterials research compared with the morphogenesis of discrete freestanding nanoparticles and nanostructures. As the most common precursors for the synthesis of alumina, ammonium aluminum carbonate hydroxide (AACH or "NH_4-Dw") and boehmite (γ-AlOOH) were chosen to investigate the effects of ILs on the formation of nanoparticles with different morphologies. Moreover, NH_4-Dw and γ-AlOOH nanostructures can be converted into porous γ-Al_2O_3 nanostructures through a subsequent thermal-decomposition process, whilst preserving the same morphology. Our experimental results demonstrate that the effects of ILs can be divided into cationic- or anionic-dominant effect models, as determined by the different surface structures of the target compounds. Specifically, under the cationic-dominant regime, ILs mainly show dispersion effects for NH_4-Dw nanostructures that can be controlled by adjusting the positions of the substituents and the length of the side-chain on the imidazole ring. In contrast, the anionic-dominant model can induce the self-assembly of γ-AlOOH particles into hierarchical structures, which can be optimized by an appropriate choice of the anions of ILs for coordination ability and hydrophilicity. To the best of our knowledge, this is the first attempt to investigate the influence of different effect models of ILs on the formation of nanoparticles with different morphologies in one reaction system. We believe that the better understanding of the influence of effect models of ILs on the formation of nanostructures is of fundamental importance. Furthermore, we hope that these findings will aid in the design of new synthetic methods for the preparation of inorganic materials by using ILs.

Results and Discussion

Previously, we reported the synthesis of aluminum acetate hydroxide ($(CH_3COO)_2Al(OH)$) nanostructures with various morphologies by using an ionic-liquid-assisted hydrothermal synthetic method with [Bdmim]Cl as the template; moreover, boehmite nanostructures can be obtained by calcination of the precursors at 300 °C.[54] However, the synthetic strategy required subsequent heat treatment, which made the synthetic route more complex. Herein, we show that the introduction of ammonium carbonate ($(NH_4)_2CO_3$) as the precipitant instead of potassium acetate (CH_3COOK) can better control the growth of NH_4-Dw and γ-AlOOH at relatively low temperatures. Scheme 1 shows a summary of the reaction conditions that were used and the corresponding results. It is reasonable to speculate that the phase and structures of the final products are mainly determined by the reaction temperature and the IL concentration: The reaction temperature is the dominant factor for the phase transformation from NH_4-Dw into γ-AlOOH in the nucleation process and the IL concentration can affect the subsequent crystal-growth process. Specifically, the effect of an IL can be divided into two aspects: Dispersion effects for NH_4-Dw and directing effects for γ-AlOOH hexagonal plates to form hierarchical structures, as a result of different effect models between the IL and the target products with different surface structures. Such interactions between ILs and the target products are helpful for understanding and the rational design of ILs that contain specific functional groups,

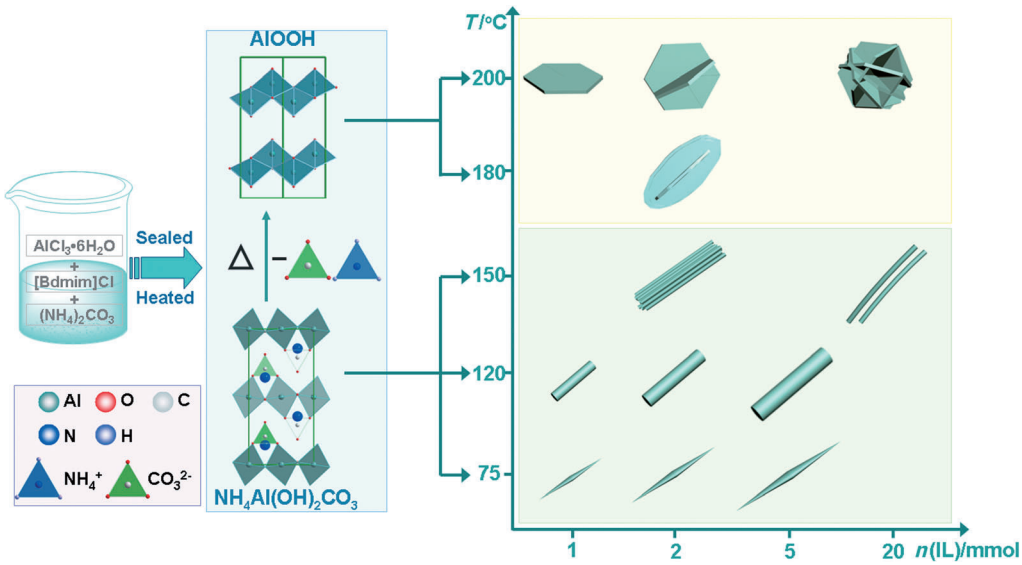

Scheme 1. Schematic representation of the formations of NH_4-Dw and γ-AlOOH nanostructures with various morphologies at different reaction temperature and IL concentrations.

thus opening up new opportunities for the synthesis of inorganic nanomaterials with new morphologies and improved properties.

Phase transformation and morphology evolution—effect of the reaction temperature: The phase and purity of the as-prepared NH_4-Dw and γ-AlOOH structures with different morphologies at different reaction temperatures were characterized by powder XRD, as shown in Figure 1. It is evident that all of the diffraction peaks in Figure 1 A, B can be perfectly indexed to the orthorhombic structure of $NH_4Al(OH)_2CO_3$ with lattice constants $a=6.618$ Å, $b=11.944$ Å, $c=5.724$ Å (JCPDS Card No. 42-0250) and to the orthorhombic structure of γ-AlOOH with lattice constants $a=3.7$ Å, $b=12.227$ Å, $c=2.868$ Å (JCPDS Card No. 21-1307), respectively. FTIR spectroscopy was performed to reveal the chemical composition and bonding situation in NH_4-Dw and γ-AlOOH crystals. The Supporting Information, Figure S2a, shows a typical FTIR spectrum of the as-prepared NH_4-Dw samples. The bond at around 3452 cm^{-1} is assigned to the stretching vibration of the O–H group. The peaks at 3020 and 3175 cm^{-1} correspond to symmetric bending stretching vibrations of NH_4^+ and the peak at about 1828 cm^{-1} is due to asymmetric bending modes. The presence of CO_3^{2-} in the as-prepared sample is evidenced by its fingerprint peaks of D_{3h} symmetry at 1547, 853, and 742 cm^{-1}, which are assigned to ν_3(E′), ν_2(A1“), and ν_4(E”), respectively, as vibrational modes according to normal modes of vibration of planar CO_3^{2-}; the peak at 2844 cm^{-1} is also commonly associated to a vibrational mode of the carbonate anion. The peaks at 755 and 623 cm^{-1} should be ascribed to Al–O lattice vibrations. The spectrum of γ-AlOOH shows absorptions that are due to various bond vibrations (see the Supporting Information, Figure S2b). The peaks at 3434 and 3160 cm^{-1} can be assigned to the υ_{as}(Al)O–H and υ_s(Al)O–H stretching vibrations, respectively. The weak bonds at 2096 cm^{-1} can be assigned to a combination band. The peak at 1064 cm^{-1} and the shoulder at 1112 cm^{-1} are ascribed to the δ_s Al–O–H and δ_{as} Al–O–H bending vibrations in the boehmite lattice. The peaks at 756 and 625 cm^{-1} can be assigned to the vibration mode of the AlO_6 octahedron. In addition, the shoulder at 1630 cm^{-1} can be assigned to the bending mode of adsorbed water. Similar FTIR spectroscopic features have previously been reported for NH_4-Dw and γ-AlOOH.[55–59] Consequently, FTIR analysis also confirmed that the as-obtained products were phase-pure.

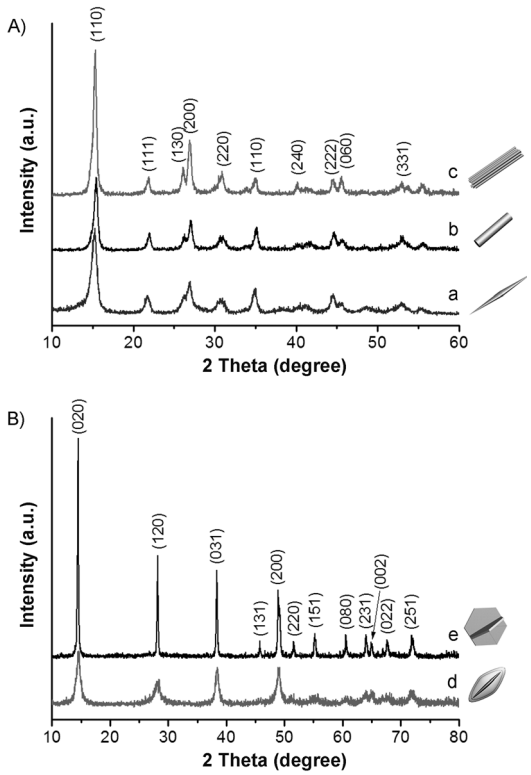

Figure 1. XRD patterns of the as-synthesized precursors at different reaction temperatures at a molar ratio of $AlCl_3 \cdot 6H_2O$ to [Bdmim]Cl of 1:1. A) NH_4-Dw: a) S-1, 75 °C; b) S-2, 120 °C; c) S-3, 150 °C. All of the diffraction peaks in the XRD patterns can be indexed to the orthorhombic structure of $NH_4Al(OH)_2CO_3$ (JCPDS Card No. 42-0250). B) γ-AlOOH: d) S-7, 180 °C; e) S-9, 200 °C. All of the diffraction peaks in the XRD patterns can be indexed to the orthorhombic structure of AlOOH (JCPDS Card No. 21-1307).

SEM images were recorded to further examine the representative morphologies of the as-prepared NH_4-Dw and γ-AlOOH at increasing reaction temperatures, as shown in Figures 2 and 3, respectively. NH_4-Dw nanoleaves were obtained at a relatively low reaction temperature, 75 °C. Figure 2 A shows a typical large-area SEM image of sample S-1, which indicates the presence of homogeneous, well-shaped nanoleaves. High-magnification SEM analysis (Figure 2 B) clearly showed the formation of NH_4-Dw nanoleaves with widths within the range 100–120 nm, lengths within the range 1.8–2 μm, and thicknesses within the range 20–30 nm. Increasing the reaction temperature to 120 °C afforded NH_4-Dw nanorods (S-2) with diameters of 15 nm and lengths of 300 nm (Figure 2 C, D). Most of the nanorods exhibited monodispersive characteristics, although a few were attached to each other side by side. However, on further increasing the reaction temperature to 150 °C, we obtained hierarchical NH_4-Dw products that were composed of large-scale bundled-wire-like nanostructures (S-3, Figure 2 E). Figure 2 F shows a typical individual bundle of nanowires with a diameter of 1 μm that exhibited the detailed structural information of bundled nanowires, that is, the bundle was actually composed of hundreds of nanowires with diameters of about 20 nm. When the reaction temperature was increased further, spindle-like and cross-plate-like γ-AlOOH nanostructures were observed at 180 and 200 °C, respectively (Figure 3). Low-magnification SEM analysis (Figure 3 A) showed that sample S-7 was composed of well-dispersed 3D spindle-like assemblies that consisted of some well-aligned nanoflakes with spindle-like edges with thicknesses of about 10 nm and lengths of about 1 μm (Figure 3 B). Moreover, the γ-AlOOH cross-plates (S-9) are micro-sized and are

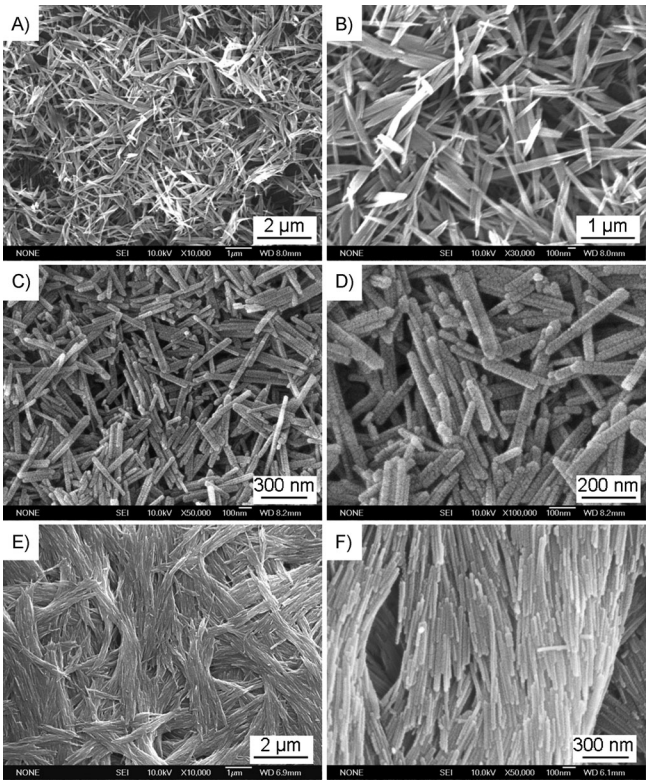

Figure 2. Low- and high-magnification SEM images of as-synthesized NH_4-Dw with different morphologies at a molar ratio of $AlCl_3{\cdot}6H_2O$ to [Bdmim]Cl of 1:1: A, B) S-1, nanoleaves; C, D) S-2, nanorods; E, F) S-3, bundles of nanowires.

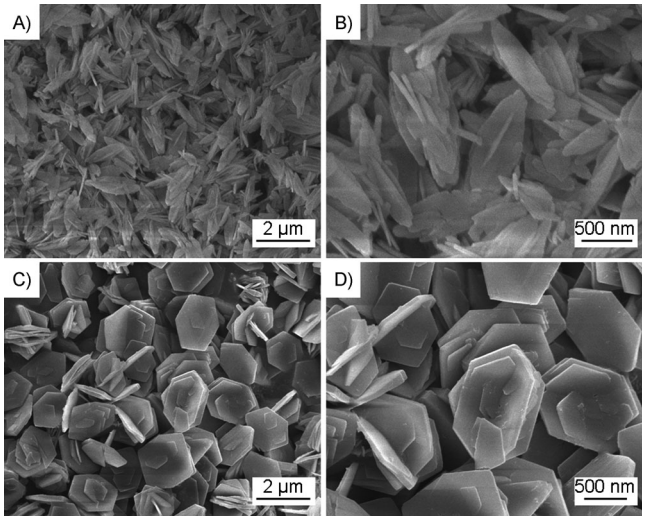

Figure 3. Low- and high-magnification SEM images of as-synthesized γ-AlOOH with different morphologies at a molar ratio of $AlCl_3{\cdot}6H_2O$ to [Bdmim]Cl of 1:1: A, B) S-7, spindles; C, D) S-9, cross-plates.

comprised two of hexagonal plates with thicknesses of about 50 nm and lengths of about 800 nm (Figure 3 C, D). The hexagonal plates are aligned perpendicular to each other to form the 3D cross-plate-like microstructures.

Notably, the only difference between these samples was the reaction temperature, which implies that the temperature of the reaction system may play an important role in tuning the phase and morphology of the particles. To investigate the effect of the reaction temperature on the formation of the particles with different phases and shapes, a series of time-dependent experiments were performed at the same reaction temperature (200 °C). The evolution of structure and morphology were elucidated by XRD and SEM, as shown in Figures 4 and 5, respectively. As reported previously, $AlCl_3$ could react with [Bdmim]Cl to form a $[Bdmim]^+{-}AlCl_4^-$ complex, which was stable at lower temperatures and gradually released $AlCl_4^-$ ions with increasing temperature (Equations (1) and (2)). When an aqueous solution of $(NH_4)_2CO_3$ was added dropwise into the reaction system (Equations (3) and (4), a creamy white solution was obtained. Upon heating the reaction medium up to a sufficiently high temperature, the reactants were chemically transformed into active atoms or ions to form the original nuclei, which can be expressed as in Equations (1)–(7).

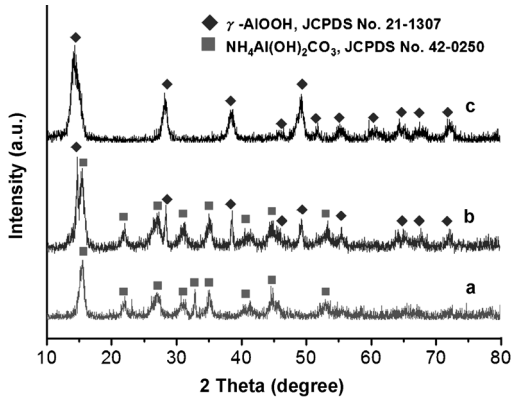

Figure 4. XRD patterns of γ-AlOOH hexagonal plates (S-8) after different reaction times: a) 1 h; b) 4 h; c) 6 h.

$$AlCl_3[Bdmim]Cl \rightarrow [Bdmim]^+{-}AlCl_4^- \quad (1)$$

$$[Bdmim]^+{-}AlCl_4^- \rightarrow [Bdmim]^+ + Al^{3+} + 4\,Cl^- \quad (2)$$

$$(NH_4)CO_3 \rightarrow 2\,NH_4^+ + CO_3^{2-} \quad (3)$$

$$CO_3^{2-} + H_2O \rightarrow HCO_3^- + OH^- \quad (4)$$

$$Al^{3+} + 2\,OH^- + H_2O \rightarrow AlO(OH)_2^- + 2\,H^+ \quad (5)$$

$$NH_4 + AlO(OH)_2^- + HCO_3^- \rightarrow NH_4Al(OH)_2CO_3 + OH^- \quad (6)$$

$$NH_4Al(OH)_2CO_3 \rightarrow AlOOH + NH_3 + CO_2 + H_2O \quad (7)$$

It should be mentioned that the $(NH_4)_2CO_3$ that is used in this synthesis mainly serves as a source of carbonate and hydroxy anions and ammonium cations, as shown in Equations (3) and (4). In the presence of a weakly basic reaction

system (pH 8.6), which is attributed to the hydrolysis of carbonate, the $AlO(OH)_2^-$ ion is considered as the main form of elemental aluminum in solution (Equation (5)), which can easily react with NH_4^+ and HCO_3^- to form NH_4-Dw (Equation (6)).[56,60] Upon gradually increasing the reaction temperature to 200 °C, within the first hour, NH_4-Dw is the dominated phase, owing to the low energy of the reaction system, as shown in Figure 4a. As is well-known, dawsonite (denoted Dw) is the mineralogical nomenclature of alkali metal hydroxyaluminocarbonate and is described by the general chemical formula $MAl(CO_3)(OH)_2$, in which "M" is an alkali metal ion (Na^+, K^+, or NH_4^+).[61,62] Structurally, NH_4-Dw consists of chains of $AlO_2(OH)_4$ octahedra that are linked by shared oxygen atoms through strong covalent bonds, with the CO_3 and NH_4 groups attached to two adjacent $AlO_2(OH)_4$ octahedra through hydrogen bonds, as shown in the Supporting Information, Figure S3.[63] The orthorhombic NH_4-Dw cell parameters of the three orthogonal directions are quite different to each other, which promotes the favored growth along a defined direction. Thus, the assembly of nanowires (Figure 5A) and the 1D growth

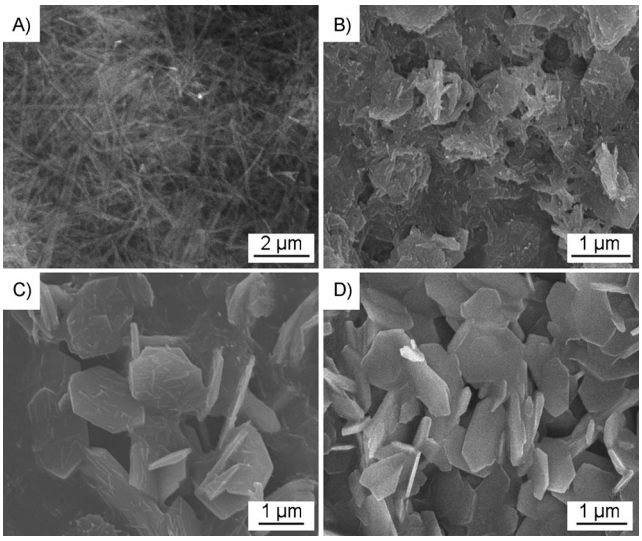

Figure 5. SEM images of γ-AlOOH hexagonal plates (S-8) after different reaction times: A) 1 h; B) 2 h; C) 4 h; D) 6 h.

behavior can be explained by the crystal nature and the growth situation. Different from the common Na-Dw, which is composed of edge-sharing $AlO_2(OH)_4$ and $NaO_4(OH)_2$ octahedra, the NH_4 group is located between Al–O chains that are associated through weak hydrogen bonds. When the reaction temperature is maintained at 200 °C, the weak hydrogen bonds that are associated with the NH_4 and CO_3 groups are broken, with the emission of NH_3, CO_2, and water, thus leaving gaps between the chains of $AlO_2(OH)_4$ octahedra as the main framework, which remains intact. Owing to the active dangling bonds and the high energy of the reaction system, the re-nucleation of γ-AlOOH occurred, accompanied by the dissolution of the NH_4-Dw nanowires. This initial transformation of phase and morphology can be detected by XRD and SEM, as shown in Figures 4b and 5B,C. After hydrothermal treatment for 4 h, the XRD pattern showed the presence of both NH_4-Dw and γ-AlOOH phases, thus indicating a phase transformation of NH_4-Dw into γ-AlOOH. From the SEM images, it can be clearly seen that the NH_4-Dw nanowires gradually dissolve to form the hexagonal skeleton (Figure 5B), thereby eventually leading to the formation of γ-AlOOH hexagonal plates with residual nanorods that are not completely dissolved on the surface (Figure 5C). On prolonging the reaction time to 6 h, the XRD pattern only shows pure γ-AlOOH (Figure 4c), thus indicating a complete phase transformation into γ-AlOOH (Equation (7)). As a boehmite structure, γ-AlOOH consists of edge-sharing Al–O octahedra, in which the oxygen atoms that are near to the middle of the layer are common to four octahedrons and correspond to O atoms, whilst the outer oxygen atoms are common to two octahedrons and correspond to OH groups (see the Supporting Information, Figure S4). The continuous parallel layers are held together through hydrogen bonds. This structure reveals that the interactions along the *a–c* plane should be stronger than the interaction between the two octahedral double layers.[64–66] Thus, the crystal grows along the *a–c* plane instead of perpendicular to it, thereby leading to the formation of γ-AlOOH hexagonal plates that inhibit the direction perpendicular to the (010) crystal plane (Figure 5D). On the basis of the above structural analysis, XRD, and SEM observations, we can conclude that the formation of γ-AlOOH under the experimental conditions can be divided into two stages: 1) The formation of NH_4-Dw nanowires at low reaction temperatures and 2) their conversion into γ-AlOOH hexagonal plates at high reaction temperatures. Overall, our proposed reaction mechanism (Scheme 2) is able to successfully explain the transformation in the phase and morphology between NH_4-Dw and γ-AlOOH.

Different effect models of ionic liquids in the synthesis of NH_4-Dw and γ-AlOOH—cationic versus anionic dominant: As shown in Scheme 1, it should be noted that, in addition to the reaction temperature, another important factor in determining the final morphology of the products is the concentration of [Bdmim]Cl. On increasing the concentration of [Bdmim]Cl, two converse roles of [Bdmim]Cl were demonstrated, owing to the presence of different substrates. Thus, we can conclude that there are different effect models of [Bdmim]Cl in the syntheses of NH_4-Dw and γ-AlOOH. According to classical surface chemistry, when liquid molecules are confined between two flat surfaces on the nanometer scale, ordered or layered structures that result in a liquid density oscillation are often formed in the vicinity of a solid/liquid boundary.[67–69] Unlike typical molecules, ILs have a highly ionic nature; thus, the ions of ILs could strongly interact with the nanoparticles to facilitate a remarkably well-defined layered structure on the charged surfaces of the particles. Moreover, ILs can form extended hydrogen-bond systems in the liquid state and, therefore, are highly structured on the surface of the nanoparticles. At this point, we can be

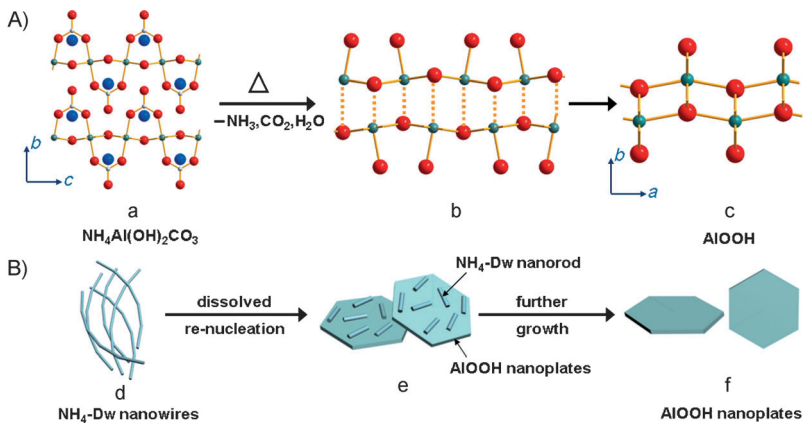

Scheme 2. Phase transformation from NH_4-Dw into γ-AlOOH: A) structure evolution and B) shape evolution.

convinced that the different effect models of [Bdmim]Cl on the formation of NH_4-Dw and γ-AlOOH are attributed to their different surface structures and charges. Similar to mineral oxides, the surface charge on dawsonite and boehmite originates from the protonation or deprotonation of the surface hydroxy groups. Both the sign and the magnitude of the surface charge depend on the pH value of the solution.[70,71] In particular, the relative population of positive and negative sites on the particle surface is equal at the point of zero charge (PZC), thereby resulting in surface-charge neutrality. This feature of pH-dependent charge has led to different types of charge on the surfaces of NH_4-Dw and γ-AlOOH, thus triggering the corresponding effect models with [Bdmim]Cl. Considering that ILs are composed of cations and anions, it is easy to understand that the types of charges on the surface of the nanoparticles will affect the cations or anions of ILs that prefer to react with the nanoparticles. In view of this property, the effect of ILs can be divided into two aspects: Cationic-dominant or anionic-dominant effects.

Dispersion of ionic liquids in the synthesis of NH_4-Dw—cationic-dominant model: To investigate the effect model of ionic liquid [Bdmim]Cl on the formation of NH_4-Dw, two control experiments were performed by using S-1 as an example. In the first experiment, a series of time-dependent experiments were performed whilst keeping the other experimental conditions the same. XRD patterns of the obtained NH_4-Dw nanoparticles were similar after different times (see the Supporting Information, Figure S5) and they could be easily indexed to the orthorhombic structure of $NH_4Al(OH)_2CO_3$ (JCPDS Card No. 42-0250). However, prolonging the reaction time can result in an improvement in the XRD pattern, which is reflected by an enlargement in the peak intensity and simultaneous decrease in their widths, thus suggesting the coarsening of the NH_4-Dw crystals. The corresponding time-dependent SEM images also clearly show the coarsening process from irregular small particles to a leaf-like structure (see the Supporting Information, Figure S6). In addition, the pH values of the reaction medium are within the range 8.6–9.1 (see the Supporting Information, Figure S7), thus resulting in negatively charged NH_4-Dw particles, owing to its low PZC (about 7.0).[72] Thus, $[Bdmim]^+$ ions can preferably adsorb onto the surface of the NH_4-Dw particles and have an effect on the formation of NH_4-Dw nanostructures, termed the cationic-dominant model.

To elucidate the exact role that was played by [Bdmim]Cl, another experiment was performed at a different concentration of [Bdmim]Cl. Clearly, the aspect ratio of NH_4-Dw nanoleaves changed significantly at higher [Bdmim]Cl concentration (see the Supporting Information, Figure S8). In the absence of [Bdmim]Cl, only irregular, ill-shaped NH_4-Dw nanoparticles were formed with lengths of less than 150 nm. Thus, the existence of [Bdmim]Cl must be key to controlling the aspect ratio of the NH_4-Dw nanoleaves. On one hand, [Bdmim]Cl could react with $AlCl_3$ to form a $[Bdmim]^+$–$AlCl_4^-$ complex, which can slowly release Al^{3+} ions to generate NH_4-Dw nuclei, thus resulting in more-uniform nanoleaves in the final product. On the other hand, $[Bdmim]^+$ ions can be easily adsorbed onto the O^{2-}-terminated surface of NH_4-Dw particles through electrostatic forces, based on the above analysis, and, more importantly, hydrogen bonds can be induced between the hydrogen atoms of the C-2 methyl groups on the imidazole rings and the bridging oxygen atoms of NH_4-Dw particles along the *c* axis. As reported previously, $[Bdmim]^+$ ions have a very strong tendency to self-assemble into ordered structures that are stabilized by additional π–π interactions along the aligned hydrogen bonds.[54] For this reason, $[Bdmim]^+$ ions can strongly interact with the surface and align perpendicular to the NH_4-Dw particles (Scheme 3), thus promoting the preferential growth of NH_4-Dw particles along the *c* axis. As a result, the aspect ratio of NH_4-Dw nanoleaves can be easily adjusted by changing the concentration of [Bdmim]Cl. Similarly, this

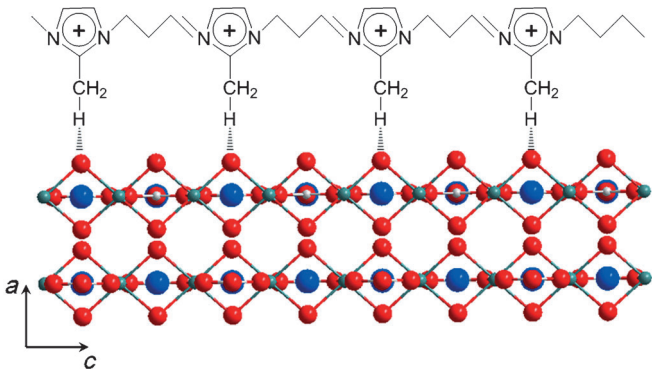

Scheme 3. Representation of $[Bdmim]^+$ ions perpendicular to the NH_4-Dw particles and their self-assembly into ordered structures along the *c* axis. Turquoise: Al^{3+}, blue: N^{3-}, gray: C^{4+}, red O^{2-}.

trend can also be reflected in the synthesis of NH_4-Dw nanorods (see the Supporting Information, Figure S9).

In particular, increasing the reaction temperature to 150 °C caused the NH_4-Dw particles to induce the growth of the free Al^{3+} ions on its negatively charged surface, owing to the high system energy during the initial stages of the reaction in the absence of [Bdmim]Cl (or low concentration of [Bdmim]Cl), thus leading to the formation of bundled-wire-like NH_4-Dw nanostructures (see the Supporting Information, Figure S10). Considering that $[Bdmim]^+$ ions can strongly interact with NH_4-Dw particles, one idea would be to use [Bdmim]Cl as a reaction medium for the dispersion of NH_4-Dw nanowire bundles. As expected, a remarkable transition from NH_4-Dw nanowire bundles into NH_4-Dw nanowires could occur with increasing concentration of [Bdmim]Cl (Figure 6). Clearly, a relatively high [Bdmim]Cl concentration (20 mmol) favors the monodisperse growth of NH_4-Dw particles, thus leading to the formation of nanowires with a diameter of 20 nm, whereas a low [Bdmim]Cl concentration does not provide enough $[Bdmim]^+$ ions to absorb onto the surface of the NH_4-Dw particles, thus retaining the NH_4-Dw nanowire bundles. However, the diameters of the nanowire bundles gradually decreases from 1.5 μm to 800 nm and 100 nm when the amount of [Bdmim]Cl increases from 2 mmol to 3 mmol and 10 mmol, respectively. This dispersion effect can be easily understood because $[Bdmim]^+$ ions interact perpendicular to the surface of the NH_4-Dw particles; thus, they can effectively prevent the free Al^{3+} ions from growing perpendicularly on the surface, thereby resulting in a morphology transition from wire bundles into wires. It should be noted that this gradual evolution is attributed to the relatively small steric bulk of the $[Bdmim]^+$ ions and to the formation of weak hydrogen bonds, thus resulting in relatively weak interactions between the $[Bdmim]^+$ ions and the NH_4-Dw particles (Scheme 4). As the "designer solvents", the interaction intensity between the IL cations and the substrate could be controlled by adjusting the position of the substituents and the length of the side-chain on the imidazole ring. When [Bmim]Cl was used instead of [Bdmim]Cl, NH_4-Dw nanowires were obtained (rather than nanowire bundles), even at low concentrations (2 mmol), which may be ascribed to the higher activity of the hydrogen atom on the C-2 position of the imidazole ring. Therefore, $[Bmim]^+$ ions can adsorb onto the surface of NH_4-Dw particles to form stronger interactions, owing to strong hydrogen bonds, thus promoting a greater dispersion effect (Figure 7 A, B). Another enhanced dispersion route is to increase the steric demands by increasing the length of the side-chain on the imidazole ring. By employing [Odmim]Cl as the reaction medium instead of [Bdmim]Cl, the $[Odmim]^+$ ions that are attached onto the surface of NH_4-Dw particles may be bulky enough to more effectively prevent the aggregation of the nanowire bundles, thus leading to the formation of NH_4-Dw nanowires at low concentrations (Figure 7 C, D). Thus, the dispersion effect of the cationic-dominant model would be optimized by an appropriate choice of the cations of the ILs, considering such affinity between the cations and the substrate surface.

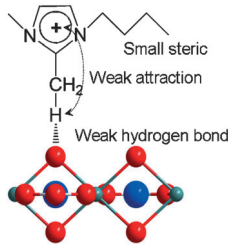

Scheme 4. Types of effects of the $[Bdmim]^+$ ions on the surface of the NH_4-Dw nanostructures. Turquoise: Al^{3+}, blue: N^{3-}, gray: C^{4+}, red O^{2-}.

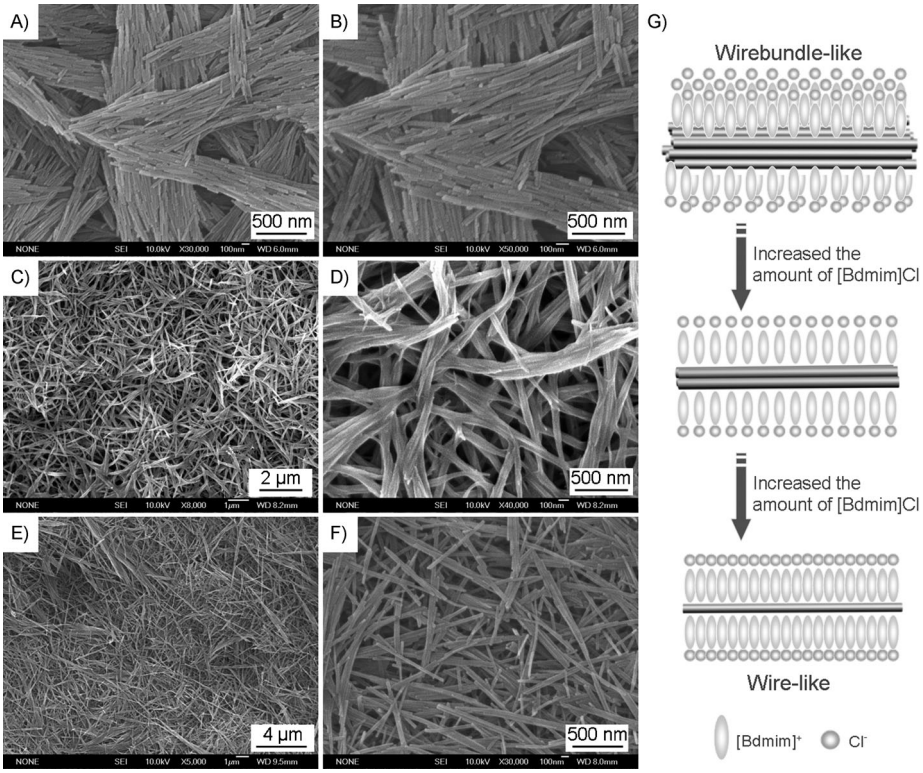

Figure 6. SEM images of NH_4-Dw nanostructures with bundled-wire-like to wire-like morphologies at different concentrations of [Bdmim]Cl: A, B) 3 mmol; C, D) 10 mmol; E, F) 20 mmol. G) Schematic representation of the shape evolution with increasing amount of [Bdmim]Cl.

Ionic-liquid-induced self-assembly of γ-AlOOH into hierarchical microstructures—anionic-dominant model: Accompanying the phase transformation from NH_4-Dw into γ-AlOOH, another effect model of [Bdmim]Cl was introduced, owing to the different surface

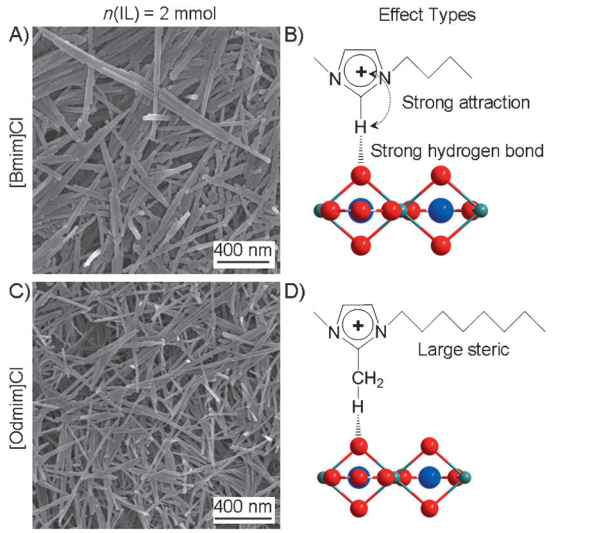

Figure 7. SEM and the corresponding schematic representation of the different effect types: A, B) S-5, [Bmim]Cl; C, D) S-6, [Odmim]Cl. Turquoise: Al^{3+}, blue: N^{3-}, gray: C^{4+}, red O^{2-}.

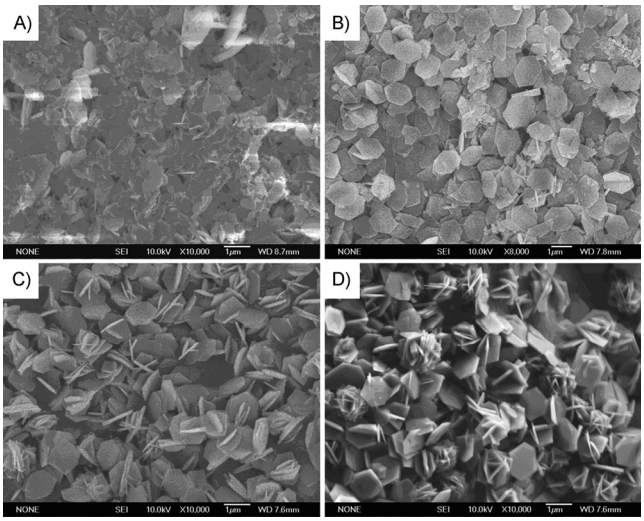

Figure 8. SEM images of γ-AlOOH microstructures with plate-like to flower-like morphologies at different concentrations of [Bdmim]Cl: A) 0 mmol; B) 1 mmol; C) 10 mmol; D) 20 mmol.

structure of the substrate. Taking γ-AlOOH hexagonal plates (S-9) as an example, unlike NH_4-Dw, the γ-AlOOH particles acquired a positive charge, owing to their high PZC (about 9.7),[50] despite being in a similar reaction medium except for a slight increase in pH value (about 9.2; see the Supporting Information, Figure S5). Thus, anions of [Bdmim]Cl will preferentially adsorb onto the building blocks of γ-AlOOH, owing to the electrostatic attractions. Then, the hydrogen bonds could occur at the interface between Cl^- ions and γ-AlOOH particles, because Cl^- ions have strong hydrophilicity and capability for hydrogen bonds, which is consistent with previous reports.[26] This effect model belongs to the anionic-dominant region, thus indicating a different effect of [Bdmim]Cl on the formation of γ-AlOOH microstructures. To further investigate the anionic-dominant effect of [Bdmim][Cl] on the formation of γ-AlOOH microstructures with various morphologies, concentration-dependent experiments were performed. Compared with the γ-AlOOH microstructures, in the absence of [Bdmim]Cl (Figure 8A), the interactions between unprotected building blocks were generally not able to form uniform microplates, thus confirming that [Bdmim]Cl could affect the growth of γ-AlOOH microstructures. As mentioned above, Cl^- ions could be easily adsorbed onto the surface of γ-AlOOH particles and form hydrogen bonds. Along with the Cl^- ions, $[Bmim]^+$ ions would also adsorb onto the γ-AlOOH surface, possibly driven by electrostatic attractions, similar to the classic DLVO (Dergaugin–Landau–Verwey–Overbeek)-type coulombic-repulsion model (Scheme 5). Consequently, well-grown γ-AlOOH microstructures can be obtained in the presence of [Bdmim]Cl. On increasing the concentration of [Bdmim]Cl from 1 mmol to 2 mmol and 20 mmol, obvious morphological evolution from hexagonal plates to cross plates and flower-like structures could occur (Figure 8), thus indicating that [Bdmim]Cl

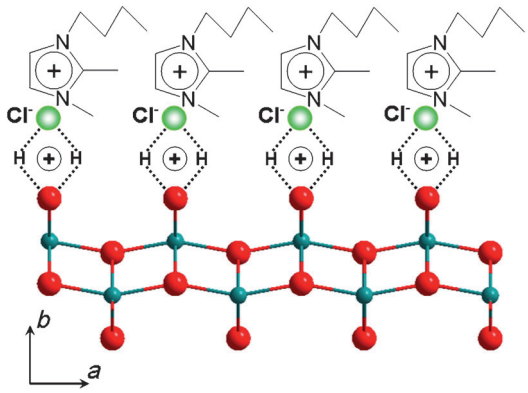

Scheme 5. Anionic-dominant model: First, the Cl^- ions of [Bdmim]Cl interact with boehmite and then the $[Bdmim]^+$ will also adsorb, driven by the electrostatic attractions. Turquoise: Al^{3+}, red O^{2-}.

may induce the self-assembly of γ-AlOOH building blocks to form hierarchical structures, which exhibit a different effect type to the previous dispersion for the synthesis of NH_4-Dw. This inducing effect could be attributed to the anionic-dominant effect model, in which Cl^- ions preferentially adsorb onto the surface of γ-AlOOH particles but do not form strong interactions with $[Bdmim]^+$ ions, so that they still can attract free Al^{3+} ions and, thus, induce the growth of Al^{3+} ions on their surface, thereby leading to the formation of hierarchical γ-AlOOH structures.

Similarly, this induction of self-assembly into hierarchical structures can be adjusted by changing the anions of the ILs. Considering that Br^- ions possess weak interactions with $[Bdmim]^+$ ions and a large size, we expected that this inducing effect may be enhanced by using [Bdmim]Br instead of [Bdmim]Cl. As predicted, larger hierarchical flower-like γ-AlOOH microstructures (about 2 μm) can be obtained at low concentrations (1 mmol; Figure 9A, B), which can be as-

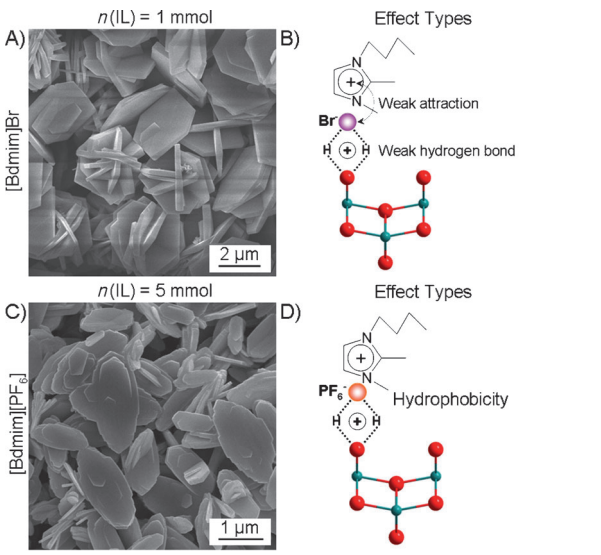

Figure 9. SEM and the corresponding schematic representation of the different effect types: A,B) S-11, [Bdmim]Br; C,D) S-12, [Bdmim][PF_6]. Turquoise: Al^{3+}, red O^{2-}.

cribed to the enhanced inducing effect. Moreover, the hydrophilicity of the anion may determine the occurrence of the induction process, because anions with strong hydrophilicity can easily attract Al^{3+} ions and induce the self-assembly. When hydrophilic [Bdmim]Cl was replaced by hydrophobic [Bdmim][PF_6], the inducing effect was inhibited. Only poorly grown plate-like γ-AlOOH microstructures could be obtained, even at a high [Bdmim][PF_6] concentration (5 mmol; Figure 9 C,D).

To shed light on the interactions between [Bdmim]Cl and NH_4-Dw or γ-AlOOH nanostructures, FTIR spectra of the as-prepared IL-hybrid samples were recorded because FTIR spectroscopy has been shown to be able to detect the existence of hydrogen bonds. As shown in the Supporting Information, Figure S11a, the bands at 3103 and 3150 cm^{-1} can be assigned to the stretching vibrations of the imidazole ring of [Bdmim]Cl, when [Bdmim]Cl is immobilized on NH_4-Dw or γ-AlOOH nanostructures, the peaks of the stretching vibration of the imidazole ring become round and weak and are shifted to lower wavenumbers, owing to the presence of less electron density because of polarization through hydrogen-bonding interactions, according to previous reports,[24,26,44] thus indicating strong interactions between [Bdmim]Cl and the NH_4-Dw or γ-AlOOH surface. However, it is difficult to use FTIR spectroscopy to differentiate between the two effect models of [Bdmim]Cl by FTIR spectroscopy, owing to the same performance of hydrogen bonds. To further investigate the difference between cationic- and anionic-dominant effect models, two control experiments were carried out. The first experiment involved replacing [Bdmim]Cl by [Bdmim]Br or [Bdmim][BF_4], whilst keeping the other experimental conditions the same (the amount of IL was 2 mmol). However, in the presence of different anions on the ILs, we still obtained the bundled-wire-like NH_4-Dw nanostructure, similar to the results in the presence of [Bdmim]Cl (see the Supporting Information, Figure S12), thus indicating that the anions of ILs had no obvious effect on the formation of the NH_4-Dw nanostructure. Compared the above results on changing the cations of ILs (Figure 7), this effect model should clearly be assigned to the cationic-dominant model. The other experiment was performed when using [Bmim]Cl or [Odmim]Cl instead of [Bdmim]Cl. Similarly, γ-AlOOH cross-plates can be obtained in spite of the presence of different cations (see the Supporting Information, Figure S13), which should be assigned to the anionic-dominant model. These control experiments demonstrate that the type of effect can be optimized by an appropriate choice of the cations or anions in the ILs, by considering the different effect models. Overall, based on our previous analysis, our proposal of the two effect models of [Bdmim]Cl (Scheme 6) is able to successfully explain the formation of NH_4-Dw and γ-AlOOH nanostructures with various morphologies.

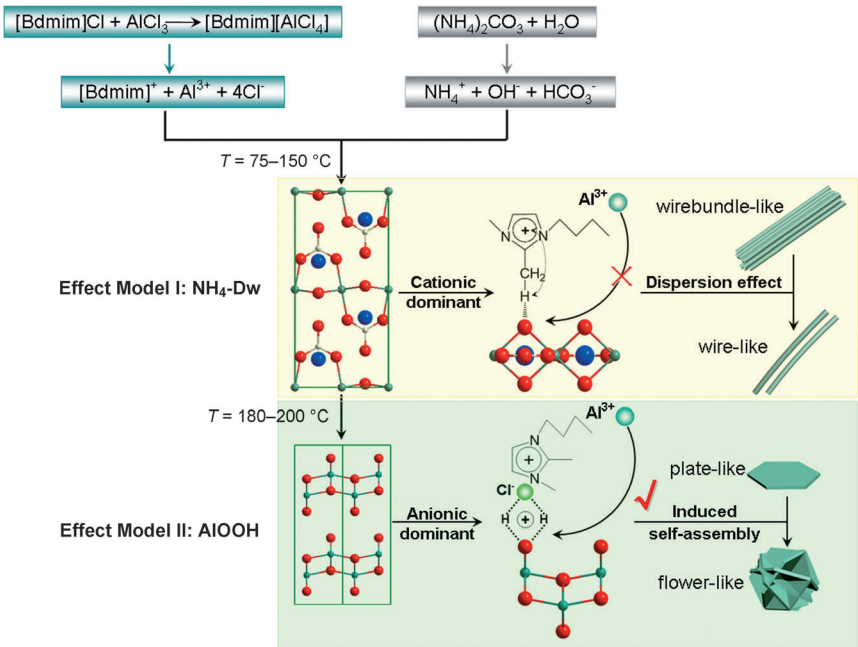

Scheme 6. The different effect models of [Bdmim]Cl in the synthesis of NH_4-Dw and γ-AlOOH. Turquoise: Al^{3+}, blue: N^{3-}, gray: C^{4+}, red O^{2-}.

Transformation of NH_4-Dw and γ-AlOOH into porous γ-Al_2O_3: As reported above, NH_4-Dw and γ-AlOOH are often used as the precursors to synthesize alumina after chemical or thermal conversion. To investigate the thermal behavior and chemical composition of the as-prepared NH_4-Dw nanowires (S-4), TG-DTA measurements were performed and the results are shown in the Supporting Information, Figure S14A. From the TG curve, the decomposition of NH_4-Dw appears to occur in three steps, with in a total weight loss of approximately 61.5% up to 720°C, slightly higher than the theoretical value (60.6%), owing to the presence of a minute amount of weakly held water molecules: The first step, from RT to 230°C, can be attributed to the decomposition of NH_4-Dw into the oxycarbonate $Al_6O_7(CO_3)_2$ (weight loss: about 52.9%); the second step, at 230–500°C, should involve the conversion of the oxycarbonate into Al_2O_3 (weight loss: about 7.4%) and the third step, at 500–720°C, should be attributed to the stripping of residual hydroxy groups on Al_2O_3 (weight loss: about 1.2%), respectively. Correspondingly, there is a sharp exothermic peak at 210°C on the DTA curve, which is associated with the decomposition of NH_4-Dw; when the temperature is above 720°C, the weight loss of the precursor no longer changes, thus indicating the transformation into a pure Al_2O_3 phase. These results are close to the previous reported results for the decomposition of NH_4-Dw.[56,62] Meanwhile, if the dehydrated precursor is considered to be γ-AlOOH (S-9), the related weight loss from RT to 850°C would be 17.8%, which is close to the theoretical value (see the Supporting Information, Figure S14B). These results were also confirmed by XRD analysis. As expected, γ-Al_2O_3 was obtained by calcination of the as-prepared precursors at 600°C for 2 h, as shown in Figure 10. All of the diffraction peaks in the XRD patterns could be indexed to the cubic structure of γ-Al_2O_3 with lattice constants $a=b=c=7.924$ Å (JCPDS Card No. 29-0063).

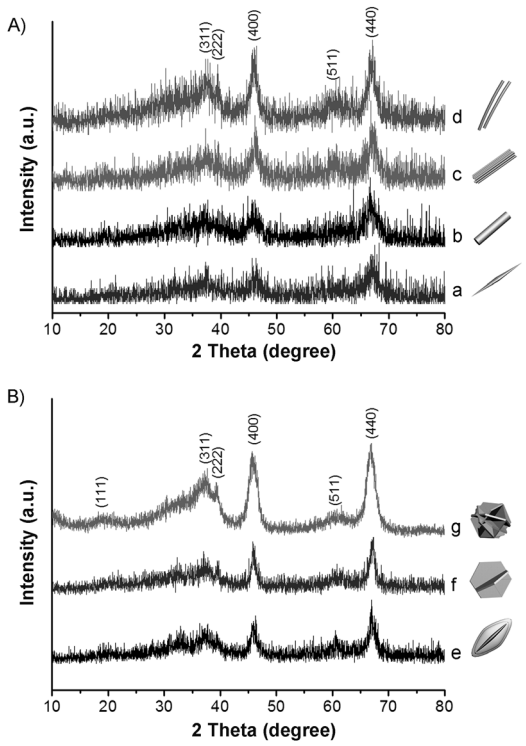

Figure 10. XRD patterns of γ-Al_2O_3 nanostructures with different morphologies that were prepared by annealing at 600°C for 2 h from A) NH_4-Dw and B) γ-AlOOH. All of the diffraction peaks in the XRD patterns can be indexed to the cubic structure of γ-Al_2O_3 (JCPDS Card No. 29-0063).

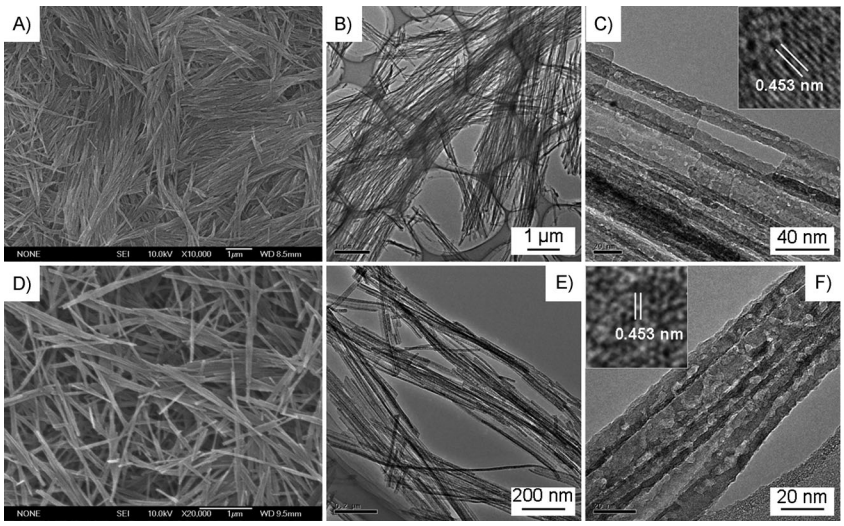

Figure 11. Representative morphologies of as-prepared γ-Al_2O_3 nanostructures: A) SEM image and B, C) TEM images of S′-3, γ-Al_2O_3 bundled nanowires; inset of panel (C) shows the corresponding HRTEM image. D) SEM image and E, F) TEM images of S′-4, γ-Al_2O_3 nanowires; inset of panel (F) shows the corresponding HRTEM image.

Further morphological and structural characterization was carried out by employing both SEM and TEM, as shown in Figures 11 and 12. Notably, the pristine morphologies of the NH_4-Dw and γ-AlOOH nanostructures were well-preserved in their calcined products and no appreciable changes in shape and size were observed. However, their surfaces seem to become rougher, based on their respective SEM images, thus indicating the generation of porous γ-Al_2O_3 through heat treatment. The corresponding TEM and HRTEM images clearly exhibited the porous features of these nanostructures. From the HRTEM images, clear lattice fringes were observed and the interplanar distance was calculated to be 0.453 nm, which corresponded to the (111) crystal planes of cubic γ-Al_2O_3. To further characterize the specific surface area and porosity of the as-pre-

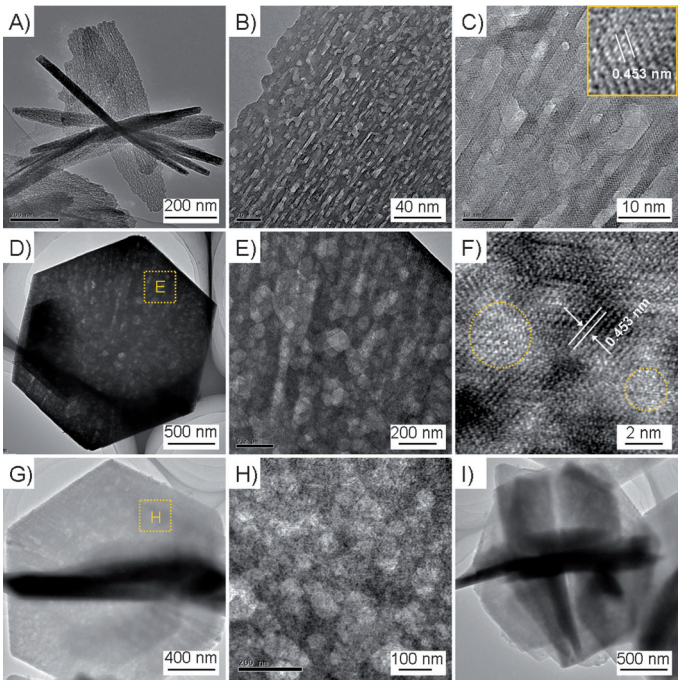

Figure 12. Representative morphologies and structures of as-prepared γ-Al_2O_3 nanostructures: A, B) TEM images and C) the corresponding HRTEM image of S′-7, spindle-like γ-Al_2O_3 microstructures; D, E) TEM images and F) corresponding HRTEM image of S′-8, hexagonal γ-Al_2O_3 microplates; G, H) TEM images of S′-9, cross-like γ-Al_2O_3 microplates; I) TEM image of S′-10, flower-like γ-Al_2O_3 hierarchical microstructures.

pared γ-Al_2O_3 samples, nitrogen-adsorption analysis was carried out. The Supporting Information, Figure S17, shows the N_2-adsorption/desorption isotherms and the corresponding pore-size-distribution curves for the γ-Al_2O_3 samples that were obtained by calcination of the different precursors at 600 °C. Clearly, all of the nitrogen-adsorption isotherms are type-IV, according to IUPAC classification.[73] These isotherms show a stepwise behavior and end at the high relative pressure of a hysteresis loop, thus reflecting a nonuniformity in the pore openings, which are associated with pore constrictions and/or ink-bottle pores with narrow necks. From the corresponding pore-size distribution, we can conclude that are two types of pores that originate from different types of aggregation in the γ-Al_2O_3 samples: 1) Mesopores (about 30 nm), which are formed between primary crystallites, and 2) macropores (about 70 nm), which are formed between secondary aggregated particles for the formation of hierarchical structures (bundle-wire-like and flower-like). These results are consistent with the high-magnification TEM images. The pore-structure parameters of the as-prepared γ-Al_2O_3 samples are listed in the Supporting Information, Table S2, which shows that the obtained γ-Al_2O_3 samples have high surface areas and excellent porous properties. Therefore, these γ-Al_2O_3 nanostructures have diverse morphologies, high crystallinity, and good textural properties and, thus, may find promising applications in high-temperature environments, such as catalysis, gas sensors, and adsorption.[74,75] In this respect, the as-prepared γ-Al_2O_3 samples were used as adsorbents to test for their potential applications in water treatment. Methyl orange (MO) was chosen as the adsorption pollutant because it is a common azo dye in the textile industry. A comparative study was performed under the same experimental conditions for the adsorption of MO by using as-prepared γ-Al_2O_3 and commercial Al_2O_3. As shown in the Supporting Information, Figure S18, all of the as-prepared γ-Al_2O_3 nanostructures exhibited better adsorption performance of MO than commercial Al_2O_3. In particular, the γ-Al_2O_3 nanowires had the best adsorptive performance, which may be ascribed to their porous structure and large specific surface area (258.49 $m^2 \cdot g^{-1}$).

Conclusion

In summary, we have successfully prepared NH_4-Dw and γ-AlOOH nanostructures with controlled morphologies by using an ionic-liquid-assisted hydrothermal route. Our experimental results demonstrate that the phase and structures of the final products are mainly determined by the reaction temperature and the concentration of [Bdmim]Cl: 1) The reaction temperature is the dominant factor in the phase transformation from NH_4-Dw into γ-AlOOH through a nucleation process and 2) the concentration of [Bdmim]Cl can affect the subsequent crystal-growth process. Specifically, the effects of the ILs can be divided into two aspects, that is, dispersion effects for NH_4-Dw (cationic-dominant model) and directing effects for γ-AlOOH hexagonal plates to form hierarchical structures (anionic-dominant model), as a result of different effect models between the ILs and the target products with different surface structures. The effects of the ILs on the formation of NH_4-Dw and γ-AlOOH nanostructures can be controlled by an appropriate choice of the anions on the ILs. Moreover, porous γ-Al_2O_3 nanostructures can be obtained by the thermal conversion of the as-prepared NH_4-Dw and γ-AlOOH nanostructures, whilst preserving the same morphology. The high crystal uniformity and excellent porous properties of the as-prepared γ-Al_2O_3 samples might have a broad range of applications, such as adsorption and catalysis.

Experimental Section

Materials: 1-butyl-2,3-dimethylimidazolium chloride ([Bdmim]Cl), 1-butyl-2,3-dimethylimidazolium bromide ([Bdmim]Br), 1-butyl-2,3-dimethylimidazolium hexaflurorophosphate ([Bdmim][PF_6]), 1-*n*-butyl-3-methylimidazolium chloride ([Bmim]Cl), and 1-octyl-2,3-dimethylimidazolium chloride ([Odmim]Cl) were obtained from Lanzhou Greenchem ILS (LICP, CAS, China). Other chemicals were purchased and used without further purification. Deionized water was used throughout.

Synthesis of NH_4-Dw and γ-AlOOH nanostructures: In a typical procedure, $AlCl_3 \cdot 6H_2O$ (2.0 mmol) and [Bdmim]Cl (2 mmol) were dissolved in deionized water (5 mL) under stirring to form a homogenous solution. Subsequently, an aqueous solution of $(NH_4)_2CO_3$ (0.60 M, 10 mL) was added dropwise into the above homogenous solution under continuous stirring. After stirring for 10 min, the solution was transferred into a

stainless-steel autoclave with a capacity of 20 mL, sealed, and heated at the set temperature for 12 h. When the reaction was complete, the autoclave was allowed to cool to RT. The resultant product was collected and washed several times with deionized water and anhydrous ethanol until the solution reached neutral pH. The final product was dried under vacuum at 60 °C for 3 h. Changing the reaction temperature and the concentration of [Bdmim]Cl could produce NH_4-Dw and γ-AlOOH with different sizes and morphologies. To investigate the effect of the ionic liquid, [Bdmim]Cl, on the synthesis, it was replaced by ionic liquids that were composed of different cations ([Bmim]Cl and [Odmim]Cl) or anions ([Bdmim]Br and [Bdmim][PF_6]), whilst keeping all of the other conditions the same. The synthetic conditions for preparing some typical samples are summarized in the Supporting Information, Table S1.

Synthesis of γ-Al_2O_3 nanostructures: Various γ-Al_2O_3 nanostructures were prepared by heating the corresponding precursors, NH_4-Dw and γ-AlOOH, at 600 °C inside an electric furnace for 2 h, followed by natural cooling to RT. The heating was performed in air and the heating rate was 2 °C min^{-1}.

Adsorption experiments of methyl orange (MO): Measurement of the adsorption performance was performed by adding the as-prepared γ-Al_2O_3 nanostructures (100 mg) into a solution of MO (100 mL, 100 mg L^{-1}) under vigorous stirring at RT. Analytical samples were removed from the suspension after various adsorption times and separated by centrifugation. The concentration of MO was analyzed by UV/Vis spectroscopy. The characteristic absorption of MO at around 465 nm was chosen to monitor the adsorption process.

Characterization: The products were characterized by X-ray diffraction (XRD), SEM, TEM, high-resolution TEM (HRTEM), FTIR spectroscopy, TGA, and BET measurements. XRD measurements were performed on a Rigaku D/max 2500 diffractometer with Cu Kα radiation (λ = 0.154056 nm) at V = 40 kV and I = 150 mA (scanning speed: 8° min^{-1}). Morphology observations were performed on a Hitachi S4800 field-emission scanning electron microscope (FESEM). TEM and HRTEM images were recorded on a Tecnai G2 20S-Twin transmission electron microscope at an accelerating voltage of 120 kV. FTIR spectra of the samples (KBr pellets) were recorded at RT on a VECTOR-22 (Bruker) spectrometer within the range 400–4000 cm^{-1}. TGA experiments (Du Pont Instruments 951 thermogravimetric analyzer) were performed on a sample (100 mg) from RT to 700 °C under a flow of nitrogen gas at a heating rate of 5 °C min^{-1}. N_2-adsorption/desorption isotherms were collected at liquid-nitrogen temperature on a Quantachrome Nova 2000e sorption analyzer. The specific surface area (SBET) of the samples was calculated by following the multipoint Brunauer–Emmett–Teller (BET) procedure.

Acknowledgements

This work was supported by the National Natural of Science Foundation of China (Grant No. 20971070 and 21073095) and by the 111 Project (B12015).

[1] J. S. Wilkes, M. J. Zaworotko, *J. Chem. Soc. Chem. Commun.* **1992**, 965–967.
[2] M. Antonietti, D. Kuang, B. Smarsly, Y. Zhou, *Angew. Chem.* **2004**, *116*, 5096–5100; *Angew. Chem. Int. Ed.* **2004**, *43*, 4988–4992.
[3] A. Taubert, Z. Li, *Dalton Trans.* **2007**, 723–727.
[4] J. A. Dahl, B. L. S. Maddux, J. E. Hutchison, *Chem. Rev.* **2007**, *107*, 2228–2269.
[5] C. Aliaga, C. S. Santos, S. Baldelli, *Phys. Chem. Chem. Phys.* **2007**, *9*, 3683–3700.
[6] H. Weingärtner, *Angew. Chem.* **2008**, *120*, 664–682; *Angew. Chem. Int. Ed.* **2008**, *47*, 654–670.
[7] R. Morris, *Chem. Commun.* **2009**, 2990–2998.
[8] Z. Ma, J. Yu, S. Dai, *Adv. Mater.* **2010**, *22*, 261–285.
[9] T. Torimoto, T. Tsuda, K. Okazaki, S. Kuwabata, *Adv. Mater.* **2010**, *22*, 1196–1221.
[10] J. Dupont, *Acc. Chem. Res.* **2011**, *44*, 1223–1231.
[11] S. Dai, Y. H. Ju, H. J. Gao, J. S. Lin, S. J. Pennycook, C. E. Barnes, *Chem. Commun.* **2000**, 243–244.
[12] J. Dupont, G. S. Fonseca, A. P. Umpierre, P. F. P. Fichtner, S. R. Teixeira, *J. Am. Chem. Soc.* **2002**, *124*, 4228–4229.
[13] T. Nakashima, N. Kimizuka, *J. Am. Chem. Soc.* **2003**, *125*, 6386–6387.
[14] Y. Zhou, M. Antonietti, *J. Am. Chem. Soc.* **2003**, *125*, 14960–14961.
[15] E. R. Cooper, C. D. Andrews, P. S. Wheatley, P. B. Webb, P. Wormald, R. E. Morris, *Nature* **2004**, *430*, 1012–1016.
[16] A. Taubert, *Angew. Chem.* **2004**, *116*, 5494–5496; *Angew. Chem. Int. Ed.* **2004**, *43*, 5380–5382.
[17] J. S. Lee, X. Wang, H. Luo, G. A. Baker, S. Dai, *J. Am. Chem. Soc.* **2009**, *131*, 4596–4597.
[18] H. Wang, J. Wang, S. Zhang, X. Xuan, *J. Phys. Chem. B* **2008**, *112*, 16682–16689.
[19] X. C. Duan, X. D. Liu, Q. Chen, H. Li, J. Li, X. Hu, Y. Li, J. M. Ma, W. J. Zheng, *Dalton Trans.* **2011**, *40*, 1924–1928.
[20] L. S. Ott, M. L. Cline, M. Deetlefs, K. R. Seddon, R. G. Finke, *J. Am. Chem. Soc.* **2005**, *127*, 5758–5759.
[21] H. J. Ryu, L. Sanchez, H. A. Keul, A. Raj, M. R. Bockstaller, *Angew. Chem.* **2008**, *120*, 7751–7755; *Angew. Chem. Int. Ed.* **2008**, *47*, 7639–7643.
[22] C. Bouvy, G. A. Baker, H. Yin, S. Dai, *Cryst. Growth Des.* **2010**, *10*, 1319–1322.
[23] W. Zheng, X. Liu, Z. Yan, L. Zhu, *ACS Nano* **2009**, *3*, 115–122.
[24] Y. Zhou, J. H. Schattka, M. Antonietti, *Nano Lett.* **2004**, *4*, 477–481.
[25] Y. Khare, Z. Li, A. Mantion, A. A. Ayi, S. Sonkaria, A. Voelkl, A. F. Thünemann, A. Taubert, *J. Mater. Chem.* **2010**, *20*, 1332–1339.
[26] H. Park, S. H. Yang, Y. S. Jun, W. H. Hong, J. K. Kang, *Chem. Mater.* **2007**, *19*, 535–542.
[27] N. Sieffert, G. Wipff, *J. Phys. Chem. C* **2008**, *112*, 19590–19603.
[28] X. Duan, J. Lian, J. Ma, T. Kim, W. Zheng, *Cryst. Growth Des.* **2010**, *10*, 4449–4455.
[29] X. Zhao, W. Jin, J. Cai, J. Ye, Z. Li, Y. Ma, J. Xie, L. Qi, *Adv. Funct. Mater.* **2011**, *21*, 3554–3563.
[30] T. Kim, W. Kim, S. Hong, J. Kim, K. Suh, *Angew. Chem.* **2009**, *121*, 3864–3867; *Angew. Chem. Int. Ed.* **2009**, *48*, 3806–3809.
[31] H. S. Park, B. G. Choi, S. H. Yang, W. H. Shin, J. K. Kang, D. Jung, W. H. Hong, *Small* **2009**, *5*, 1754–1760.
[32] W. Yang, T. P. Fellinger, M. Antonietti, *J. Am. Chem. Soc.* **2011**, *133*, 206–209.
[33] W. Dobbs, J. Suisse, L. Douce, R. Welter, *Angew. Chem.* **2006**, *118*, 4285–4288; *Angew. Chem. Int. Ed.* **2006**, *45*, 4179–4182.
[34] Z. Li, P. Rabu, P. Strauch, A. Mantion, A. Taubert, *Chem. Eur. J.* **2008**, *14*, 8409–8417.
[35] H. Park, Y. Lee, B. G. Choi, Y. S. Choi, J. Yang, W. H. Hong, *Chem. Commun.* **2009**, 4058–4060.
[36] N. Recham, L. Dupont, M. Courty, K. Djellab, D. Larcher, M. Armand, J. M. Tarascon, *Chem. Mater.* **2009**, *21*, 1096–1107.
[37] M. Armand, F. Endres, D. R. MacFarlane, H. Ohno, B. Scrosati, *Nat. Mater.* **2009**, *8*, 621–629.
[38] Z. Li, A. Geßner, J. Richters, J. Kalden, T. Voss, C. Kübel, A. Taubert, *Adv. Mater.* **2008**, *20*, 1279–1285.
[39] J. P. Paraknowitsch, J. Zhang, D. Su, A. Thomas, M. Antonietti, *Adv. Mater.* **2010**, *22*, 87–92.
[40] Z. Zhang, T. Pinnavaia, *J. Am. Chem. Soc.* **2002**, *124*, 12294–12301.
[41] H. C. Lee, H. J. Kim, S. H. Chung, K. H. Lee, H. C. Lee, J. S. Lee, *J. Am. Chem. Soc.* **2003**, *125*, 2882–2883.
[42] Y. Li, Y. Bando, D. Golberg, *Adv. Mater.* **2005**, *17*, 1401–1405.
[43] X. S. Fang, C. H. Ye, L. D. Zhang, T. Xie, *Adv. Mater.* **2005**, *17*, 1661–1665.
[44] H. S. Park, Y. S. Choi, Y. M. Jung, W. H. Hong, *J. Am. Chem. Soc.* **2008**, *130*, 845–852.
[45] H. S. Park, Y. S. Choi, Y. Kim, W. H. Hong, H. J. Song, *Adv. Funct. Mater.* **2007**, *17*, 2411–2418.
[46] H. K. Farag, F. Endres, *J. Mater. Chem.* **2008**, *18*, 442–449.
[47] S. C. Shen, Q. Chen, P. S. Chow, G. H. Tan, X. T. Zeng, Z. Wang, R. B. H. Tan, *J. Phys. Chem. C* **2007**, *111*, 700–707.

[48] L. Zhang, Y. J. Zhu, *J. Phys. Chem. C* **2008**, *112*, 16764–16768.
[49] X. Yu, J. Yu, B. Cheng, M. Jaroniec, *J. Phys. Chem. C* **2009**, *113*, 17527–17535.
[50] W. Cai, J. Yu, M. Jaroniec, *J. Mater. Chem.* **2010**, *20*, 4587–4594.
[51] D. Kuang, Y. Fang, H. Liu, C. Frommen, D. Fenske, *J. Mater. Chem.* **2003**, *13*, 660–662.
[52] W. Lee, R. Scholz, U. Gösele, *Nano Lett.* **2008**, *8*, 2155–2160.
[53] J. Lian, J. Ma, X. Duan, T. Kim, H. Li, W. Zheng, *Chem. Commun.* **2010**, *46*, 2650–2652.
[54] T. Kim, J. Lian, J. Ma, X. Duan, W. Zheng, *Cryst. Growth Des.* **2010**, *10*, 2928–2933.
[55] C. J. S. Serna, J. V. Garcia-Ramos, M. J. Pena, *Spectrochim. Acta Part A* **1985**, *41*, 697–702.
[56] A. A. Ali, M. A. Hasan, M. I. Zaki, *Chem. Mater.* **2005**, *17*, 6797–6804.
[57] G. Stoica, J. C. Groen, S. Abelló, R. Manchanda, J. Pérez-Ramírez, *Chem. Mater.* **2008**, *20*, 3973–3982.
[58] J. Zhang, S. Liu, J. Lin, H. Song, J. Luo, E. M. Elssfah, E. Ammar, Y. Huang, X. Ding, J. Gao, S. Qi, C. Tang, *J. Phys. Chem. B* **2006**, *110*, 14249–14252.
[59] J. Zhang, S. Wei, J. Lin, J. Luo, S. Liu, H. Song, E. Elawad, X. Ding, J. Gao, S. Qi, C. Tang, *J. Phys. Chem. B* **2006**, *110*, 21680–21683.
[60] G. Stoica, J. Pérez-Ramírez, *Chem. Mater.* **2007**, *19*, 4783–4790.
[61] L. B. Railsback, *Carbonates Evaporites* **1999**, *14*, 1–20.
[62] M. J. Hernandez, M. A. Ulibarri, J. Cornejo, M. J. Pena, C. J. Serna, *Thermochim. Acta* **1985**, *94*, 257–266.
[63] E. Corazza, C. Sabelli, S. Vannucci, *Neues Jahrb. Mineral. Monatsh.* **1977**, *9*, 381–397.
[64] X. Krokidis, P. Raybaud, A. Gobichon, B. Rebours, P. Euzen, H. Toulhoat, *J. Phys. Chem. B* **2001**, *105*, 5121–5130.
[65] M. Digne, P. Sautet, P. Raybaud, H. Toulhoat, E. Artacho, *J. Phys. Chem. B* **2002**, *106*, 5155–5162.
[66] D. Chiche, C. Chizallet, O. Durupthy, C. Chanéac, R. Revel, P. Raybaud, J. Jolivet, *Phys. Chem. Chem. Phys.* **2009**, *11*, 11310–11323.
[67] K. Ueno, M. Watanabe, *Langmuir* **2011**, *27*, 9105–9115.
[68] J. N. A. Canongia Lopes, A. A. H. Pádua, *J. Phys. Chem. B* **2006**, *110*, 3330–3335.
[69] A. Triolo, O. Russina, H. J. Bleif, E. D. Cola, *J. Phys. Chem. B* **2007**, *111*, 4641–4644.
[70] I. Larson, C. J. Drummond, D. Y. C. Chan, F. Grieser, *J. Am. Chem. Soc.* **1993**, *115*, 11885–11890.
[71] J. C. Schulz, G. G. Warr, *Langmuir* **2002**, *18*, 3191–3197.
[72] G. A. Parks, *Chem. Rev.* **1965**, *65*, 177–198.
[73] K. S. W. Sing, D. H. Everett, R. A. W. Haul, L. Moscou, R. A. Pierotti, J. Rouquérol, T. Siemieniewska, *Pure Appl. Chem.* **1985**, *57*, 603–619.
[74] H. Park, Y. Lee, B. G. Choi, Y. S. Choi, W. H. Hong, J. Yang, *ChemSusChem* **2008**, *1*, 356–362.
[75] H. Park, Y. Lee, B. G. Choi, Y. S. Choi, J. Yang, W. H. Hong, *Small* **2010**, *6*, 290–295.

Received: September 7, 2012
Published online: March 11, 2013

